The Astrophysical Journal, 693:597–609, 2009 March 1 doi:10.1088/0004-637X/693/1/597

RADIATIVE OPACITY OF IRON STUDIED USING A DETAILED LEVEL ACCOUNTING MODEL

Fengtao Jin[1,2], Jiaolong Zeng[1], Tianxuan Huang[2], Yongkun Ding[2], Zhijian Zheng[2], and Jianmin Yuan[1]
[1] Department of Physics, National University of Defense Technology, Changsha 410073, People's Republic of China; jmyuan@nudt.edu.cn
[2] Research Center of Laser Fusion, China Academy of Engineering Physics, Mianyang 621900, People's Republic of China
Received 2008 June 16; accepted 2008 November 10; published 2009 March 2

ABSTRACT

The opacity of iron plasma in local thermodynamic equilibrium is studied using an independently developed detailed level accounting model. Atomic data are generated by solving the full relativistic Dirac–Fock equations. State mixing within one electronic configuration is considered to include part of the correlations between electrons without configuration interaction matrices that are too large being involved. Simulations are carried out and compared with several recent experimental transmission spectra in the *M*- and *L*-shell absorption regions to reveal the high accuracy of the model. The present model is also compared with the OPAL, LEDCOP and OP models for two isothermal series at $T = 20$ eV and $T = 19.3$ eV. It is found that our model is in good agreement with OPAL and LEDCOP while it has discrepancies with OP at high densities. Systematic Rosseland and Planck mean opacities in the range 10–1000 eV for temperature and 10^{-5}–10^{-1} g cm^{-3} for density are also presented and compared with LEDCOP results, finding good agreement at lower temperatures but apparent differences at high temperatures where the *L*- and *K*-shell absorptions are dominant.

Key words: atomic data – atomic processes – methods: data analysis

Online-only material: color figures

1. INTRODUCTION

Opacity dominates the radiative transfer within plasmas and consequently has a strong influence on radiative hydrodynamic evolution. In astrophysical studies, stellar opacity controls radiative energy transport, governs the flow of fusion energy from core to exterior, and affects stellar structure and evolution. Although iron is only present in stellar envelopes at the level of a few percent, its bound–bound (b–b) and bound–free (b–f) absorptions have proved to be very important to the envelope opacity (Simon 1982; Rogers & Iglesias 1994). In recent studies, the Fe I b–f opacity was also found to be important to the "missing UV opacity" in the solar atmosphere (Bell et al. 2001; Castelli & Kurucz 2004). In the past two decades, many statistical and detailed opacity models (Rogers & Iglesias 1992; Iglesias & Rogers 1996; Magee & Clark 1999; Seaton et al. 1994; Hummer et al. 1993; Jin et al. 2003; Zeng & Yuan 2004) have been developed to investigate the contribution of iron line absorption to stellar opacities. Lawrence Livermore National Laboratory (LLNL) developed a detailed term accounting (DTA) model called OPAL (Rogers & Iglesias 1992; Iglesias & Rogers 1996) to perform new calculations of stellar opacities. The OPAL calculations showed that the *M*-shell $\Delta n = 0$ transitions of iron, which had been ignored in the old Los Alamos National Laboratory (LANL) opacities (Cox & Tabor 1976), would significantly increase the stellar opacities. OPAL opacities had been successfully applied in studies of the classical Cepheids. Nowadays more theoretical work has been done to calculate accurate opacities of stellar mixtures, such as the LEDCOP and ATOMIC codes of LANL (Magee & Clark 1999[3]; Fontes et al. 2006) and the international collaborations of the Opacity Project (OP; Seaton 1987; Seaton et al. 1994; Seaton &Badnell 2004) and the Iron Project (Hummer et al. 1993). Though OP and OPAL are different in their calculation of atomic data and equation of state (EOS), the two sets of opacities are in good general agreement except for regions of high density and temperature. In more recent works (Seaton & Badnell 2004; Badnell et al. 2005) the agreement between OP and OPAL was improved by introducing inner-shell processes into the OP atomic data.

To check the theoretical models, many experimental measurements have been made in the open *M*-shell regime. Earlier iron experiments focused on the $3p \rightarrow 3d$ transitions at relatively low temperatures. Winhart et al. (1995, 1996) performed a measurement in the spectral range 70–140 eV at a temperature of 22 eV and a density of 0.01 g cm^{-3}. Springer et al. (1997) measured a transmission spectrum of iron plasma near the critical region of stellar envelopes at a temperature of 20 eV and a density of 10^{-4} g cm^{-3}. Chenais-Popovics et al. (2000) measured the iron spectrum in the $2p \rightarrow 3d$ energy region at a temperature of 20 eV. Recently, Foord et al. (2004) measured the *L*-shell absorption lines to diagnose the charge state distributions in an iron plasma. Most recently, Bailey et al. (2007) measured the iron *L*-shell opacities at the Sandia National Laboratory Z-pinch facility. The iron plasmas were heated to very high temperatures above 150 eV and at an electron density of $6.9 \pm 1.7 \times 10^{21}$ cm^{-3}, which are very close to the conditions of the solar radiation convection boundary. The experimental spectra were well characterized to provide benchmark data for the validation of the theoretical models.

Several theoretical methods such as the average atom (AA) model, the unresolved transition array (UTA) model, the supertransition array (STA) model, and the detailed level accounting (DLA) model have been developed. The AA model is the simplest; it averages all the ionic states in a plasma to a fictitious ion with shell structures. The electrons are then distributed to the shells according to the Fermi–Dirac distribution method. The UTA and STA methods are detailed configuration accounting models, in which groups of lines belonging to the same or neighboring transition arrays are approximated by single Gaussians. The AA, UTA, and STA methods are also referred

[3] More details of the LEDCOP code are available from http://www.t4.lanl.gov and access the opacity data via the TOPS server.

to as statistical models, and they can rapidly compute opacities, especially of high-Z materials. But they are poor at interpreting detailed line structures of experimental spectra. The DLA model is a so-called line-by-line model, where the atomic configurations split into terms or levels and each line in the transition array is calculated. In contrast to the statistical methods, the DLA model can calculate more accurate opacities but requires much more effort in computing atomic data, especially in studies of medium- and high-Z materials.

We perform detailed studies of iron opacities using an independently developed DLA model in local thermodynamic equilibrium (LTE). The huge number of atomic data are obtained by solving the full relativistic Dirac–Fock equation. In b–b calculations j–j couplings of configurations are considered. State mixing within one electronic configuration is considered to partly take the electronic correlations into account in order to avoid large-scale configuration interaction (CI) matrices of open M-shell configurations. In the b–f calculations configuration splitting is not considered. To examine the model's accuracy, calculations are carried out and compared with several experimental transmission spectra of iron plasmas at low and high temperatures. Systematic Rosseland and Planck mean opacities in the temperature range 10–1000 eV and the density range 10^{-5}–10^{-1} g cm^{-3} are also provided and compared with the results of OPAL, LEDCOP, and OP.

2. METHOD OF THE DLA MODEL

The calculation of opacity requires large numbers of atomic data, such as atomic energy levels, oscillator strengths, photoionization cross sections, free–free absorption cross sections, photon scattering cross section by free electrons, and transition line shapes, as well as the populations both between and within ionization stages.

2.1. Radiative Opacity and Population

In LTE, the total absorption to a photon with energy $h\nu$ in a plasma is

$$\rho\kappa\left(h\nu\right) = \left[\mu_{\rm bb}\left(h\nu\right)+\mu_{\rm bf}\left(h\nu\right)+\mu_{\rm ff}\left(h\nu\right)\right] \times\left(1-e^{-h\nu/kT}\right)+\mu_s, \quad (1)$$

where κ_ν is the total opacity at the photon energy $h\nu$, ρ is the mass density of the plasma, T is the temperature, and k is the Boltzmann constant. $\mu_{\rm bb}$, $\mu_{\rm bf}$, and $\mu_{\rm ff}$ are the absorption coefficients of the bound–bound (b–b), bound–free (b–f), and free–free (f–f) transitions, respectively. μ_s is the scattering cross section of a photon by free electrons.

The b–b absorption coefficient for a photon with energy $h\nu$ is calculated by

$$\mu_{\rm bb}\left(h\nu\right)=\sum_i\left[\sum_{ll'}N_{il}\sigma_{ill'}\left(h\nu\right)\right], \quad (2)$$

where N_{il} is the population of level l of ionization stage i. $\sigma_{ill'}$ is the cross section of the b–b transition from level l to l' and is calculated by the formula

$$\sigma_{ill'}\left(h\nu\right)=\frac{\pi he^2}{m_ec}f_{ill'}S\left(h\nu\right), \quad (3)$$

where $S\left(h\nu\right)$ is the line shape function, $f_{ill'}$ is the oscillator strength from level l to l', h is the Planck constant, e is the electron charge, m_e is the electron mass, and c is the speed of light. In the present work, we consider both Stark broadening and Doppler broadening. The Doppler half width at half maximum (HWHM; Cowan 1981) is given by

$$\Gamma_d = 3.858\times10^{-5}\left(kT/A\right)^{1/2}\left(h\nu_0\right), \quad (4)$$

where A is the atomic weight of the ion and kT, $h\nu_0$, and Γ_d are in eV. The Stark HWHM is expressed as a semiempirical formula (Dimitrijevic & Konjevic 1987)

$$\Gamma_l = N_e\frac{4\pi}{3}\frac{\hbar^3}{m^2e}\left(\frac{2m}{\pi kT}\right)^{1/2}\frac{\pi}{\sqrt{3}}\left(0.9-\frac{1.1}{z}\right) \times\sum_{j=i,f}\left(\frac{3n_j}{2z}\right)^2\left(n_j^2-l_j^2-l_j-1\right), \quad (5)$$

where n_i, n_j, l_i, l_j are the principal and angular quantum numbers of the initial and final orbitals related to the transition, and N_e is the electron number density. The line shape function $S\left(h\nu\right)$ is applied with the Voigt profile

$$S\left(h\nu\right)=\frac{\sqrt{\ln2}}{\sqrt{\pi}\Gamma_d}H\left(a,v\right), \quad (6)$$

in which $H\left(a,v\right)$ is the Voigt function

$$H\left(a,v\right)=\frac{a}{\pi}\int_{-\infty}^{+\infty}\frac{e^{-x^2}}{a^2+\left(v-x\right)^2}dx, \quad (7)$$

where $a=\sqrt{\ln2}\Gamma_l/\Gamma_d$ and $v=\sqrt{\ln2}\left(h\nu-h\nu_0\right)/\Gamma_d$.

In the calculation of the b–f opacity we applied a detailed configuration accounting (DCA) model (Rose 1992). The total b–f absorption cross section of ion i is a weighted sum running over all bound states that are explicitly considered

$$\sigma_{\rm bf}^i\left(h\nu\right)=\frac{\pi he^2}{m_ec}\sum_\alpha P_i\left(\alpha\right)\frac{df_{\alpha\to c}}{d\left(h\nu\right)}, \quad (8)$$

where $df_{\alpha\to c}/d\epsilon$ is the one-configuration photoionization oscillator density and $P_i\left(\alpha\right)$ is the relative probability of configuration α calculated by the Saha–Boltzmann equations. Then the total b–f absorption coefficient of the plasma is written as

$$\mu_{\rm bf}\left(h\nu\right)=\sum_i N_i\sigma_{\rm bf}^i\left(h\nu\right). \quad (9)$$

Except for very low energy photons, the f–f contribution is very small in contrast to the b–b and b–f absorptions; then the Kramers (Rose 1992) cross section is used

$$\sigma_{\rm ff}\left(h\nu\right)=\frac{16\pi^2e^2h^2}{3\sqrt{3}c\left(2\pi m\right)^{3/2}}\frac{z^3N_ig_{\rm ff}}{\left(kT\right)^{1/2}\left(h\nu\right)^3}, \quad (10)$$

where the f–f Gaunt factor, $g_{\rm ff}$, is taken as unity. The total f–f absorption coefficient is then written as

$$\mu_{\rm ff}\left(h\nu\right)=\sum_i N_i\sigma_{\rm ff}\left(h\nu\right). \quad (11)$$

In the present study, the temperatures of the iron plasmas considered are $\leqslant$1000 eV. At this limitation the energies of the photons, which have contributions to the mean opacities, are

much lower than the relativistic limit mc^2 (0.51 MeV). Thus, we use Thomson scattering to calculate the scattering cross section

$$\mu_s(h\nu) = N_e\sigma_s = \tfrac{8}{3}\pi r_e^2 N_e, \tag{12}$$

where $r_e = e^2/4\pi\epsilon_0 m_e c^2$ is the classical electron radius.

In LTE plasma the ionization balance can be obtained by solving the Saha equation (Xu 1986).

$$\frac{N_{i+1}N_e}{N_i} = \frac{Z_{i+1}Z_e}{Z_i}\exp[-(\phi_i - \Delta\phi_i)/kT], \tag{13}$$

where N_e and N_i are the electron and ion number densities. ϕ_i and $\Delta\phi_i$ are the ionization potential and the so-called ionization potential depression (IPD). Z_i and Z_e are the partition functions of ions and free electrons, respectively. They are defined as

$$Z_i = \sum_l g_{il} e^{-E_{il}/kT} \tag{14}$$

and

$$Z_e = 2\left(\frac{2\pi m_e kT}{h^2}\right)^{3/2}, \tag{15}$$

where E_{il} is the energy of level l relative to the ground state of ion i, and $g_{il} = 2J + 1$ is the degeneracy. Then the population of level l is determined by the Boltzmann distribution

$$N_{il} = g_{il}\,(N_i/Z_i)\,e^{-E_{il}/kT}. \tag{16}$$

The sum of Equation (14) runs over all bound states of ion i and is truncated at the ionization threshold, which has been lowered by $\Delta\phi_i$.

In a plasma of high density, the energy levels of one atom will be perturbed by the neighboring ions and free electrons. We take these effects into account as the so-called IPD, which will lower the ionization potential ϕ_i by $\Delta\phi_i$. In this paper, the plasma density was limited up to 0.1 g cm^{-3}, so the Stewart–Pyatt model (Stewart & Pyatt 1966) is a good method to evaluate the IPD

$$\Delta\phi_i = \frac{\left[3\,(z^*+1)\,\frac{z_i e^2}{DkT} + 1\right]^{2/3} - 1}{2\,(z^*+1)}, \tag{17}$$

where D is the Debye length, z_i is the net charge of the ion i, and z^* is the mean ionization degree.

In hydrodynamic calculations, Rosseland and Planck mean opacities are usually used. They are defined, respectively, as

$$\frac{1}{K_R} = \int_0^\infty \frac{W_R\,(u)\,du}{\kappa\,(u)} \tag{18}$$

and

$$K_P = \int_0^\infty [\kappa\,(u) - \kappa_s\,(u)]\,W_P\,(u)\,du, \tag{19}$$

where $u = h\nu/kT$, κ_s is the scattering opacity. W_R and W_P are the Rosseland and Planck weighting functions:

$$W_R\,(u) = \frac{15}{4\pi^4}\frac{u^4 e^{-u}}{(1-e^{-u})^2}, \tag{20}$$

and

$$W_P\,(u) = \frac{15}{\pi^4}\frac{u^3 e^{-u}}{(1-e^{-u})}. \tag{21}$$

In experiments researchers do not measure the opacity directly but the transmission. The relation between opacity and transmission is defined by

$$F\,(h\nu) = e^{-\mu\kappa(h\nu)}, \tag{22}$$

where μ is the areal density of the sample. The function F is integrated over a Gaussian function with the full width corresponding to the spectrometer resolution to obtain the final transmission spectrum.

2.2. Atomic Levels and Transitions

Iron is a typical medium-Z material with an open M shell. One configuration with a partially filled $3d$ orbital could split into several thousands or even tens of thousands of j–j coupling schemes. Then multi-CI calculation may lead to overlarge matrices. Diagonals of many CI matrices with such large dimensions are very time-consuming and even impractical within the abilities of current computers. Therefore, in the present work only state mixing within one configuration is considered to partly take the electronic correlations into account. The wave function of an atom in j–j coupling is written as

$$\Psi(\gamma\,J\,M) = \sum_i c_i \Phi(\gamma_i\,J\,M), \tag{23}$$

where $\Psi(\gamma\,J\,M)$ is the atom wave function labeled by $\gamma\,J\,M$, J is the total angular momentum, $\Phi(\gamma_i\,J\,M)$ is a configuration state function (CSF) with total angular momentum J, and γ_i represents the configuration and any quantum numbers other than $J\,M$ that are needed for complete specification of the state. The sum runs over all states of the same configuration with the same $J\,M$. The CSF is a vector-coupled state of one-electron orbitals

$$\phi(njm) = \frac{1}{r}\begin{pmatrix} P_{n\kappa}(r)\chi_\kappa^m(\theta,\varphi) \\ i\,Q_{n\kappa}(r)\chi_{-\kappa}^m(\theta,\varphi)\end{pmatrix}, \tag{24}$$

where κ is the relativistic quantum number, $P_{n\kappa}(r)$ and $Q_{n\kappa}(r)$ are respectively the large and small component radial wave functions, and the functions $\chi_\kappa^m(\theta,\varphi)$ are the spinor spherical harmonics

$$\chi_\kappa^m(\theta,\varphi) = \sum_{\pm\sigma}\left\langle l, m-\sigma, \frac{1}{2}\sigma\middle| l\frac{1}{2}jm\right\rangle Y_l^{m-\sigma}(\theta,\varphi)\chi^\sigma, \tag{25}$$

where $\langle l, m-\sigma, \frac{1}{2}\sigma|l\frac{1}{2}jm\rangle$ is a Clebsch–Gordan coefficient, $Y_l^{m-\sigma}(\theta,\varphi)$ is a spherical harmonic and χ^σ is a spinor basis function. The radial wave functions $P_{n\kappa}$ and $Q_{n\kappa}$ are generated by the standard self-consistent field (SCF) method.

The eigenvalue of state Ψ_i is given by

$$E_i = \langle\Psi_i|\hat{H}|\Psi_i\rangle \tag{26}$$

and the transition probability from state Ψ_i to Ψ_j is

$$f_{ij} = \frac{(E_j - E_i)}{3(2J+1)}|\langle\Psi_j\|\mathbf{P^{(1)}}\|\Psi_i\rangle|^2, \tag{27}$$

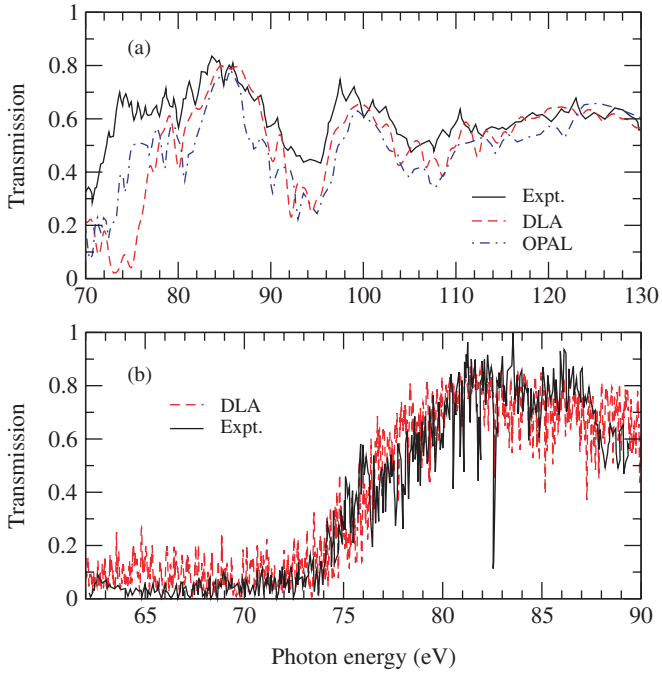

Figure 1. Comparison of iron transmission between calculation and experiment. The black line in (*a*) refers to a measurement by Winhart et al. (1995, 1996). The red and blue lines refer to the results of our DLA and OPAL at $T = 22$ eV and $\rho = 0.01$ g cm^{-3}, respectively. The black line in (*b*) refers to the measurement by Springer et al. (1997) and the red line refers to the results of our DLA at $T = 20$ eV and $\rho = 0.0001$ g cm^{-3}.

(A color version of this figure is available in the online journal.)

where f_{ij} is the oscillator strength and $\mathbf{P}^{(1)}$ is the electron dipole (E1) operator.

Since iron is a typical medium-Z material, it is very time consuming to generate the great number of levels and lines for all ionization stages. In the current work, we parallelized the GRASP code (Parpia et al. 1996) in the environment of the message passing interface (MPI), which is a set of standard code libraries supported by most parallel computers. The calculations of the transition lines from each configuration were distributed to the slave nodes and were collected by the master node. Linear efficiency with the number of computing nodes was found in our calculation.

3. RESULTS AND DISCUSSION

For convenience of comparison with experiments and other codes we refer to our results as "DLA" in the following discussions. First we examine the accuracy of our model by comparing our calculations with several recent experiments.

The black lines in Figure 1 are two experimental transmission spectra of iron in the XUV region (Winhart et al. 1995; Springer et al. 1997) while the red lines are our calculations. The absorption lines in the spectra are due to M-shell photoexcitation and photoionization of Fe VI–XI. In the calculation of the b–b transitions, all the bound configurations of one ion are taken as the initial states while the final states are produced by one-electron excitations of the initial states. Taking Fe VIII as an example, $[\mathrm{Ne}]3s^2 3p^6 3d$, $[\mathrm{Ne}]3s^2 3p^6 nl$ ($n \leqslant 9$), $[\mathrm{Ne}]3s^2 3p^5 3dnl$ ($n \leqslant 5$), $[\mathrm{Ne}]3s 3p^6 3d^2$, $[\mathrm{Ne}]3s 3p^6 3dnl$ ($n \leqslant 4$), $[\mathrm{Ne}]3s^2 3p^4 3d^2$, and $[\mathrm{Ne}]3s 3p^5 3d^3$ are selected as the initial states according to their relative energies to the ground state, and the final states are generated by exciting one M-shell electron, i.e., $3s$, $3p$, or $3d$, to the valence orbitals $n'l'$. The b–f absorptions are generated by photoionization from all the initial configurations. One can see that the configurations in the calculations may have several $3d$ electrons and therefore lead to a large number of j–j splitting levels. In fact the total number of lines of the corresponding ions involved in the calculations reached 10^8. In the cases of Figures 1(a) and (b) a total of 3.5×10^8 and 5.3×10^8 lines were used respectively in the DLA to calculate the spectrally resolved opacities in the photon energy range 0–600 eV. Table 1 shows some calculated energy levels of Fe VIII. The experimental data (Corliss & Suger 1985) and a multiconfigurational Hartree–Fock (MCHF) calculation (Jin et al. 2003), which use LS coupling with Breit–Pauli corrections, are also given for comparison. Table 1 shows that the MCHF calculation agree better with experiment than the DLA for some higher levels, but most of the energies of the MCHF and of the present DLA are slightly larger (generally by less than 4%) than the experimental ones. However, they act as a global shift from the experimental levels of about 2 eV. In Figure 1, both the DLA spectra have been shifted 2 eV downward to meet the measured ones.

In Figure 1(a), the transmission spectrum was measured in the photon energy range 70–130 eV, which corresponded to the $n = 3$ to $n = 3, 4, 5, 6$ transitions (Winhart et al. 1995). Both OPAL and our spectra are calculated at $T = 22$ eV and $\rho = 0.01$ g cm^{-3}. In this case, Fe VII and Fe VIII are the main charge states in the plasma, which are 34% and 43%

Table 1
Some Calculated Energy Levels (in cm^{-1}) of Fe VIII

Configuration	J	DLA	MCHF	Experiment
$3p^4_{3/2}3d_{3/2}$	3/2	0.0	0.0	0.0
$3p^4_{3/2}3d_{5/2}$	5/2	1975	1934	1836
$3p^3_{3/2}(3d^2_{5/2})_2$	5/2	429418	435696	431250
$3p^3_{3/2}(3d^2_{5/2})_4$	5/2	430061	436369	
$3p^3_{3/2}(3d^2_{5/2})_2$	3/2	431219	439677	
$3p^1_{1/2}3p^4_{3/2}(3d^2_{5/2})_4$	7/2	433803	439993	434555
$3p^3_{3/2}(3d^2_{5/2})_2$	1/2	439551	443121	
$3p^1_{1/2}3p^4_{3/2}(3d^2_{5/2})_2$	3/2	445509	445953	
$3p^3_{3/2}(3d^2_{5/2})_2$	7/2	460701	456069	447656
$(3p^3_{3/2}3d_{3/2})_2 3d_{5/2}$	5/2	462126	465622	459367
$3p^3_{3/2}(3d^2_{5/2})_0$	3/2	518071	519755	508518
$3p_{1/2}3p^4_{3/2}(3d^2_{5/2})_0$	1/2	528789	529111	520822
$(3p^3_{3/2}3d_{3/2})_2 3d_{5/2}$	5/2	561300	550169	535909
$(3p_{1/2}3p^4_{3/2}3d_{1/2})_1 3d_{5/2}$	7/2	567708	555261	541755
$3p^3_{3/2}3d_{1/2})_3 3d_{5/2}$	1/2	614286	609560	591964
$3p^3_{3/2}(3d^2_{5/2})_2$	3/2	617532	612548	595152
$3p^3_{3/2}(3d^2_{5/2})_4$	5/2	628672	610998	596463
$3p_{1/2}3p^4_{3/2}(3d^2_{3/2})_2$	3/2	629234	611250	597065
$3p^4_{3/2}4f_{5/2}$	5/2	766672	762179	763703
$3p^4_{3/2}4f_{7/2}$	7/2	766682	762291	763799
$(3p^3_{3/2}3d_{3/2})_0 4s_{1/2}$	1/2	840963	840465	837661
$(3p^3_{3/2}3d_{3/2})_1 4s_{1/2}$	3/2	846694	841460	842829
$(3p^3_{3/2}3d_{5/2})_4 4s_{1/2}$	9/2	847418	849074	
$(3p^3_{3/2}3d_{3/2})_3 4s_{1/2}$	7/2	850056	852776	847145
$(3p^3_{3/2}3d_{3/2})_3 4s_{1/2}$	5/2	852937	855660	849899
$(3p^1_{1/2}3p^4_{3/2}3d_{3/2})_2 4s_{1/2}$	3/2	856018	857723	852849
$(3p^3_{3/2}3d_{5/2})_4 4s_{1/2}$	7/2	859678	860029	855100
$(3p^1_{1/2}3p^4_{3/2}3d_{3/2})_2 4s_{1/2}$	5/2	865511	866205	860615

Note. Experimental data (Corliss & Suger 1985) and a MCHF calculation (Jin et al. 2003) are also given for comparisons.

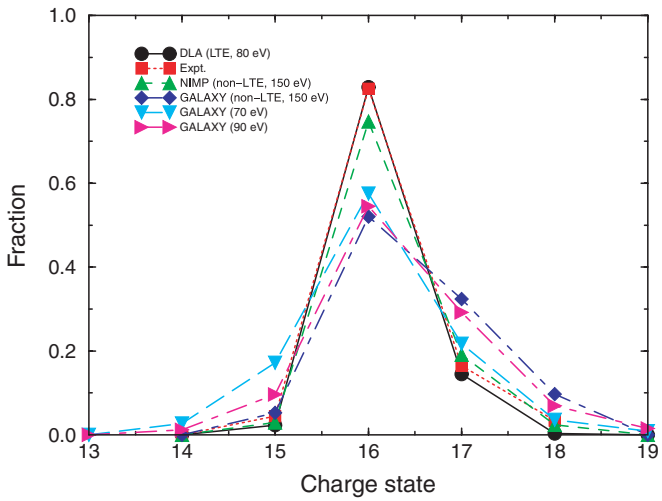

Figure 2. Charge state distribution in an iron plasma. The squares refer to the experiment of Foord et al. (2004). All theoretical results were obtained at $n_e = 2 \times 10^{19}$ cm^{-3}. The current LTE result was obtained at a temperature of 80 eV. The NIMP (Rose et al. 2004) result was obtained at an electron temperature of 150 eV. The GALAXY (Foord et al. 2004) results were obtained at electron temperatures of 70, 90, and 150 eV, respectively.

(A color version of this figure is available in the online journal.)

of the total, respectively. The absorptions in the range 70–90 eV come from the $3p \rightarrow 3d$ transitions. The absorption peak around 94 eV is mainly due to the $3p \rightarrow 4s$ and $3d \rightarrow 5f$ of Fe VII and the $3d \rightarrow 4f$ transitions of Fe VIII. The absorptions around 106 eV are due to the $3d \rightarrow 6f$ of Fe VII and $3p \rightarrow 4s$ of Fe VIII. Both our calculation and OPAL show good agreement with experiment for the main features of the spectrum. Our calculation shows better agreement with experiment in 80–130 eV than OPAL. However, all the theoretical absorptions in the range 70–80 eV were much stronger than experiment. In this range OPAL is better than our calculation. The correlation effect is one possible reason for this discrepancy. OPAL is a DTA model, which generates the atomic data by solving the single-electron Dirac equation with a parametric potential, which is determined by fitting a few existing experimental energy levels, and multi-CI are not included explicitly. Fe VII and Fe VIII configurations with M-shell vacancies could split into a large number of LS terms and many more j–j levels. State mixing is very strong both between different electronic configurations and within the same configuration. In a previous study (Jin et al. 2003; Zeng et al. 2003), we showed that the MCHF method with enough CI calculation could effectively lower the oscillator strengths of some strong $3p \rightarrow 3d$ transitions. Also, the calculated transmission in 70–80 eV agreed better with experiment. However, full CI is very difficult in j–j coupling. In future work, we plan to improve our model by considering multi-CI for the ground and low-excited configurations, in which the number of relativistic splits are not too large.

Springer et al. (1997) reported an iron opacity experiment in the $3p \rightarrow 3d$ region. The sample was kept well in LTE and reached a temperature of 20 eV and a density of 10^{-4} g cm^{-3}, which were very close to the conditions of the Cepheid variable envelopes. The high instrumental resolving power ($E/\Delta E$) was also impressive. Thus this experiment could provide direct validation of detailed theoretical models at relatively lower density. Figure 1(b) shows the comparison between the calculated spectrum and the measured one. In this case, the main species in the plasma are Fe VIII, Fe IX, Fe X, and Fe XI, with 4.4%, 36.7%, 48.7%, and 9.8% percentages of the total number of ions, respectively. The absorptions in this spectrum come from the $3p \rightarrow 3d$ transitions of these ions. In Figure 1(b), excellent agreement is achieved for the global features of the spectra. Absorption saturations are found in the range 62–73 eV in both experiment and calculation. The calculated slope in the range 73–82 eV fits the measured one very well. However, some disagreement is also found. The calculated absorptions in the range 85–88 eV appear slightly stronger than the measured absorptions. There is a strong line at 82.6 eV in the measured spectrum, stronger than the calculated one.

In a recent experiment, Foord et al. (2004) investigated the charge state distribution in a photoionized Fe/NaF plasma mixture. The measured absorptions of the iron L-shell lines were used to determine the population fractions of the charge states. The measured electron number density in the plasma sample was $n_e = 2 \times 10^{19}$ cm^{-3} and the mean charge state of iron 16.1 $\pm$ 0.2. Foord et al. (2004) and Rose et al. (2004) used several non-LTE opacity codes (GALAXY, FLYCHK, CLOUDY, and NIMP) to reproduce the measured charge state distributions of iron. However, fairly large uncertainties in the electron temperatures were found by these non-LTE codes. Also, the predictions of the Fe XVII population by these theoretical models were much lower than the measured population. Although a plasma at such a lower density is generally believed to be in non-LTE, we find that an LTE calculation could also reproduce the iron charge state distribution and fit the experimental spectrum even better than those non-LTE calculations. Figure 2 shows the iron charge state distributions obtained from experiment and from several theoretical calculations. The current LTE calculation is performed at $T = 80$ eV and $n_e = 2 \times 10^{19}$ cm^{-3} yielding a mean charge state of 16.2. In Figure 2, the populations of Fe XVI, Fe XVII, and Fe XVIII in the current calculation agree quite well with the measured ones. Among the non-LTE calculations, the result of NIMP was the best, which was very close to the experimental result. Although the GALAXY results also show good agreement with experiment, the calculated charge state distribution was rather insensitive to the electron temperature in the range 70–150 eV. Figure 3 shows the comparison between the measured iron lines and our LTE calculation. In this spectrum the lines are from the $2p \rightarrow 4d$ transitions of Fe XVIII and the $2p \rightarrow nd$ ($n = 5, 6, 7$) transitions of Fe XVII. One can see that the calculated lines agree quite well with experiment both for line positions and line strengths. In LTE plasma, the level populations obey a Boltzmann distribution, and the fractions of nearby charge states can be obtained by solving the Saha equation. In non-LTE plasma, the level populations are not in a Boltzmann distribution but are determined by the various collisional and radiative rates. The good agreement in Figure 3 indicates that at least the relative charge stage populations in the experiment are well described by solving the Saha equation. However, a Boltzmann distribution among the energy levels is usually much more easy to achieve than the relative ion charge state. It is also found that the Na and F populations cannot be reproduced at $T = 80$ eV, and the two ions should have higher effective temperatures of 99 and 85 eV, respectively. Thus the plasma mixture cannot not be described by a single LTE temperature. Busquet (1993) first introduced a technique to calculate populations in non-LTE plasma, in which the level populations were assumed to obey a Boltzmann-like law, i.e., populations varying as $e^{-\Delta E/T_z}$, where T_z was defined as the effective temperature of configurations. Klapisch & Bar-Shalom (1997) and Bauche et al. (2006) also showed that

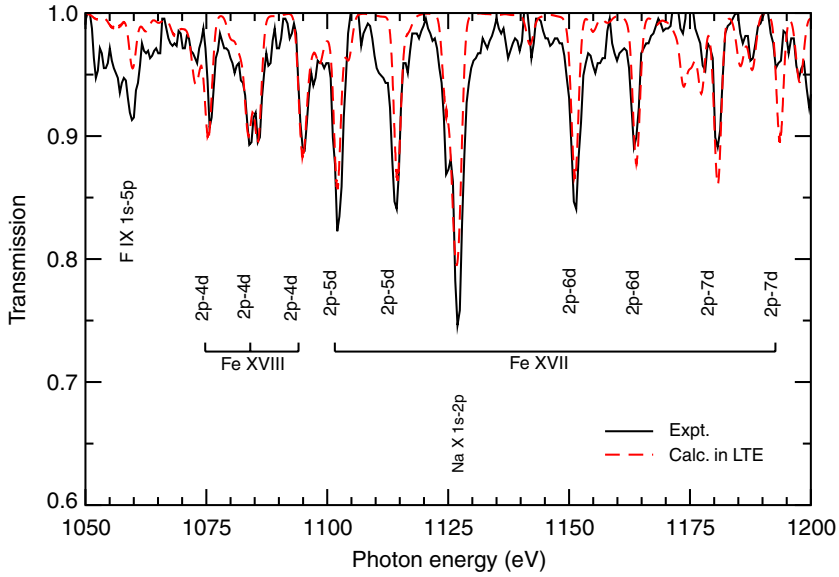

Figure 3. Transmission spectrum of an iron plasma. The black solid line refers to the experimental data of Foord et al. (2004), the red dashed line refers to the current LTE calculation at $T = 80$ eV and $n_e = 2 \times 10^{19}$ cm^{-3}.
(A color version of this figure is available in the online journal.)

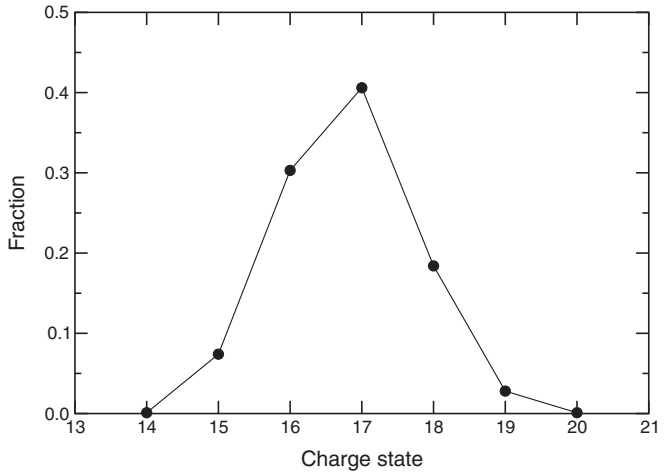

Figure 4. Calculated Fe charge state distributions in the Fe/Mg mixture at a temperature of 150 eV and electron number density of 8.5×10^{21} cm^{-3}. The mean charge state is 16.7.

the effective temperature method was an appealing and simple way to describe the populations in some non-LTE plasmas. Thus we conclude that though the Fe/NaF mixture in the experiment was not in LTE, their populations both within and between ions may still be described by a Boltzmann-like distribution with an effective temperature of 80 eV.

Most recently, Bailey et al. (2007) measured the transmission of iron plasma produced on a Z-pinch at a very high temperature of above 150 eV and an electron density of $6.9 \pm 1.7 \times 10^{21}$ cm^{-3}. Clear iron L-shell lines were measured and were reproducible from shot to shot. In the experiment, Mg was mixed into the sample to help drive the populations toward LTE. The temperatures and densities in this experiment are very close to the conditions of the solar radiation–convection boundary. Therefore, this experiment could provide good validation of modern opacity models, particularly the detailed line-by-line models. We calculated the populations and the transmissions in the Fe/Mg mixture at a temperature of 150 eV and electron density of 8.5×10^{21} cm^{-3}. The charge state distribution of iron is shown in Figure 4. At such a high temperature the L-shell electrons begin to be ionized and therefore there are vacancies in the L-shell. Figure 5 shows a comparison between the DLA and the experiment. The lines in the $h\nu < 990$ eV range were measured in thin samples of areal density 32 μg cm^{-2}, and the lines in the $h\nu > 990$ eV range were measured in thick samples of areal density 61 μg cm^{-2}. In this spectrum the lines in the range 990–1320 eV are due to $L \rightarrow N$ and $L \rightarrow O$ transitions. Although there are overlaps between these two types of transitions, the lines can be identified clearly. One can easily see that both the positions and the strengths of the calculated lines in this region show excellent agreement with the measured ones. Between 800 and 980 eV the lines come from $L \rightarrow M$ transitions. Since the L-shell electron energies of neighboring charge states have large differences, their $L \rightarrow M$ absorption lines separate clearly into a few groups. In this region the calculated lines are also in good agreement with experiment. The good agreement for the global features reveals that the calculated charge state distribution is very close to the true distribution in the experiment. It assures that the plasma sample in the experiment was kept well in LTE. However, discrepancies exist for some lines. The calculated absorptions in the range 920–930 eV are stronger than in the experiment, and the calculated line at 999 eV is weaker than the measured one. Bailey et al. (2007) also gave three detailed theoretical simulations by the PRISMSPECT, OPAL, and MUTA codes, and good agreement was found between these codes and experiment. However, similar discrepancies as in the experiment at 920–930 eV and at 999 eV were also found in the OPAL and MUTA spectra.

Chenais-Popovics et al. (2000) performed an iron opacity experiment in the $2p \rightarrow 3d$ regime. The iron plasma was heated to a temperature of about 20 eV and a density of 0.004 g cm^{-3}. The transmissions in the spectral range 721–756 eV were measured. Several opacity codes called SCO, STA, and SOSA, which are based on STA and UTA methods, were given for comparison. We calculated the iron transmission at a temperature of 20 eV and density of 0.004 g cm^{-3} to make comparisons with the experiment as well as those opacity codes in the literature (Chenais-Popovics et al. 2000). Table 2 lists the

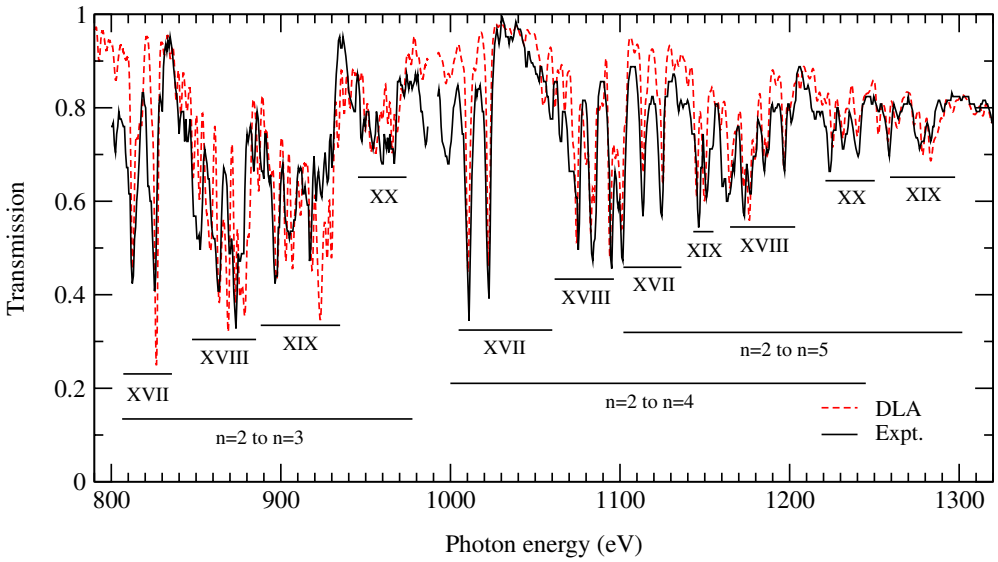

Figure 5. The black line refers to recent measurement of iron transmission by Bailey et al. (2007), and the red line refers to our simulation at 150 eV and 8.5×10^{21} cm^{-3}.

(A color version of this figure is available in the online journal.)

Table 2
Iron Populations Calculated by Several Codes at a Temperature of 20 eV and Density of 0.004 g cm^{-3} (Chenais-Popovics et al. 2000)

Ion	SCO	SOSA	OPAL	DLA
Fe VI	0.08	0.04	0.07	0.05
Fe VII	0.33	0.36	0.33	0.31
Fe VIII	0.44	0.40	0.44	0.46
Fe IX	0.12	0.14	0.13	0.17
Fe X	0.01	0.04	...	0.01

Note. DLA refers to our current calculation.

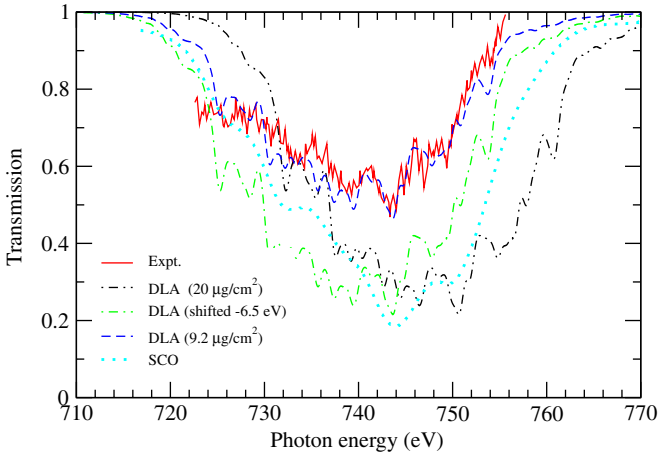

Figure 6. The red solid line refers to the measured iron transmission by Chenais-Popovics et al. (2000), and the black dot-dot-dashed line refers to the present DLA calculation at 20 eV and 0.004 g cm^{-3} with an areal density 20 μg cm^{-2}. To meet the measured data the calculated data was shifted 6.5 eV downward (green dot-dashed line) and used an areal density 9.2 μg cm^{-2} (blue dashed line). The cyan dotted line refers to the result of the SCO code (Chenais-Popovics et al. 2000).

(A color version of this figure is available in the online journal.)

ionic populations obtained by the present DLA, SCO, SOSA, and OPAL codes at the same temperature and density. One can see that the population distributions calculated by the different codes are in excellent agreement and show that Fe VII and Fe VIII are dominant ions. Figure 6 shows the comparison between the current calculation and the measured spectrum. In contrast to the spectra in the experiments of Foord et al. (2004) and Bailey et al. (2007), the spectrum in Figure 6 has few clear line structures but rather is a curve with small absorption peaks. This is because Fe VII and Fe VIII are ions with an open M-shell and there are strong overlaps among their huge numbers of $2p \rightarrow 3d$ lines. So it is difficult to identify the individual lines in the spectrum. In the present study, we calculate the transmission according to the areal density 20 μg cm^{-2} given in the literature (Chenais-Popovics et al. 2000). It is shown that the calculated absorptions (the black dot-dot-dashed line) are much stronger than in the experiment and the whole spectrum should be shifted downward by 6.5 eV (the green dot-dashed line) to meet the measured line positions. In order to fit the experimental spectrum, a transmission with a reduced areal density 9.2 μg cm^{-2} (the blue dashed line) is also calculated. After adjusting the line positions, the line strengths and the contour of the calculated spectrum are in excellent agreement with the experiment. Figure 6 also shows the spectrum calculated by the SCO code (Chenais-Popovics et al. 2000). The strength and the contour of the SCO spectrum is similar to the current DLA result except that it has fewer detailed absorption structures. To fit the experiment the areal density used in the SCO code should be lowered by a factor of 2.7, i.e., 7.4 μg cm^{-2}. The SOSA code (Chenais-Popovics et al. 2000) also showed that an areal density 12 μg cm^{-2} instead of 20 μg cm^{-2} would be more appropriate to reproduce the measured spectrum. The reasons for the discrepancies between the experiment and opacity codes are complicated. In the experiment, the effect of the second-order diffraction of the crystal and inaccurate measurement of the sample thickness could introduce uncertainties into the absorptions. In theoretical opacity models, accurate calculation of the oscillator strengths, the line broadenings, and the ionization balances are very difficult for medium- and high-Z materials. Such problems remain issues in the development of modern opacity models.

In contrast to the uncertainties in the absorption measurement, the determination of line positions is generally subject to few

experimental errors. The line position shift in the DLA spectrum is due to a deficiency in our model, in which the orbital relaxations of the final states are not considered. In order to maintain the computational stability of the energy levels and transitions, we used the same sets of electron wave functions, which are pre-optimized separately, for both initial and final states. However, when an electron in an inner shell is excited to valence orbitals the redistribution of the electrons would cause the electron wave functions of the final state to be quite different from those of the initial state. To show the orbital relaxation effects we calculated the wave functions of the initial and final $2p$ and $3d$ orbitals of the $2p \rightarrow 3d$ transition from the Fe VIII ground state and plotted them in Figure 7. Compared to the initial $3d$ orbital, the final $3d$ orbital, is contracted inward due to the reduction of the screening of the $2p$ electron to the nuclear charge, and therefore the binding energy of the final $3d$ orbital will increase. At the same time the final $2p$ orbital has few changes. Thus the $2p \rightarrow 3d$ transition energy would be too large if the orbital relaxation were not considered. Table 3 lists the energies of some Fe VIII $2p \rightarrow 3d$ transitions from the ground and low-excited states calculated both considering and not considering orbital relaxations. Orbital relaxations are considered by carrying out self-consistent field calculations for the initial and final states, respectively. From Table 3 one can see that the transition energies are decreased by including the orbital relaxations. The energy shifts of the transitions from the ground state are around 6.0 eV while the shifts from the low-excited states are about 6.5 eV. Since the transition lines from the low-excited states and the Rydberg states are numerous and dominate the main absorptions in this plasma, the DLA spectrum needs to globally shift 6.5 eV downward to meet the measured one.

However, we find that the line shifts in Figures 1, 3, and 5 are only 2 eV. In Figure 1, the plasma temperatures are also 20 eV, but the absorption lines in the plotted two spectra are due to the $3p \rightarrow 3d$ transitions. Because the screening effects among the valence shells are relatively small, the two DLA spectra need to move only 2 eV downward to meet the experimental values. In Figures 3 and 5, the lines were also from photoexcitation of the L-shell electrons; however, the DLA spectrum is found to be only a small shift of 2 eV from the measured one. In the present model, we generate the electron radial wave functions by exciting one electron from the ground configuration to each valance orbital. Unlike the experiment of Chenais-Popovics et al. (2000) the plasmas in the experiments of Foord and Bailey reached such high temperatures that the M-shell electrons were fully ionized. We generated the electron radial wave functions by exciting one $2p$ electron to each valance orbital. Thus, the orbital relaxation effects are automatically taken into account in Figures 3 and 5. At a temperature of 20 eV the shifts of the $2p \rightarrow 3d$ lines have little influence on the calculated Rosseland and Planck mean opacities, which are mainly determined by M-shell absorption. However, the large shifts could lead to misidentification of the experimental lines, and hence to errors in the temperature diagnostics of the plasmas. In addition, the influence of the orbital relaxations to the oscillator strengths also needs to be studied. We plan to perform further studies of the orbital relaxations in our future work.

In hydrodynamic researches, Rosseland and Planck mean opacities are usually used. The calculation of iron opacities is very difficult because the open M-shell of the ions can generate a huge number of levels and transitions. Statistical techniques are often used to simplify the calculation of the large number of the transition lines, such as the AA, UTA, and STA models. The fourth international opacity workshop WorkOp-IV, which was held in 1997, focused on iron opacities and summarized the results of many theoretical works (Serduke et al. 2000). It showed that the iron mean opacities of various theoretical codes had large differences, particularly for the Rosseland mean opacities at lower densities.

Figure 8 shows the mean opacities of an isothermal series at 20 eV. This series is of interest in astrophysics and is also a good validation for theoretical models due to its complexitiy. At this temperature the Rosseland and Planck weighting functions Equations (20) and (21) reach their maximum, respectively, at the photon energies of 76.6 eV and 58.8 eV, and the regions around these energies corresponds to the M-shell $\Delta n = 0$ transitions. Since the L-shell lines are far from this region their contribution to the mean opacities is negligible. In this series the mean charge state varies from 10.9 to 5.2 when the density increases from 10^{-6} g cm^{-3} to 10^{-1} g cm^{-3}, i.e., the $3p$ and $3d$ orbitals are not yet fully ionized. Billions of transition lines are involved in the calculations. In Figure 8, the results of OPAL and LEDCOP are also plotted for comparison. Good agreement is found both for the Planck and Rosseland mean opacities. At densities of 10^{-3} and 10^{-2} g cm^{-3} the OPAL Rosseland opacities are slightly lower than those of LEDCOP but are 23% and 21% larger than our results, respectively. When the density decreases to 10^{-5} and 10^{-6} g cm^{-3} the OPAL and our Rosseland opacities become larger than those of LEDCOP. At 10^{-6} g cm^{-3} our Rosseland opacity is 384 cm^2 g^{-1}, which is 28% larger than that LEDCOP. The LEDCOP Planck opacity is 29% larger than our result at 10^{-4} g cm^{-3}, but is 23% smaller than ours at 10^{-2} g cm^{-3}. The present DLA results at these two densities agree better with OPAL than with LEDCOP. The differences may be due to the different methods of the detailed treatments of the transition lines in the models. For example, LEDCOP obtained most of the atomic data by one-configuration LS Hartree–Fock schemes with relativistic corrections. In order to reduce the calculation of the huge number of transition lines, LEDCOP applied a UTA method to deal with many b–b transitions and replaced the actual transition array with a single Gaussian profile to approximate all the actual lines. Because the Rosseland mean opacity is very sensitive to the line width, the UTA treatment may lead to overestimates of the Rosseland opacities at lower densities.

Figure 9 shows the comparison between OP and the present DLA for an isothermal series of $T = 19.3$ eV. The density ranges from 8.7×10^{-7} g cm^{-3} to 0.63 g cm^{-3}. The OP opacities in Figure 9 were generated from OPCD.3.3, which is the latest opacity package (released on 2006 December 12) available for download from the TOPbase Web site (see http://cdsweb.u-strasbg.fr/topbase). Inner-shell contributions have been included in this updated version. In Figure 9, the DLA Planck mean opacities agree quite well with the OP ones below a density of 1.2×10^{-3} g cm^{-3}, while the DLA Rosseland mean opacities are slightly higher than those of OP. In Table 4, the electron densities N_e calculated by OP and DLA show little difference at lower densities. Such agreement assures that the charge state distributions calculated by the two models are the same. However, both the Planck and the Rosseland mean opacities of DLA tend to be much larger than those of OP at higher densities. The reasons for the discrepancies are rather complicated. In general, such differences could be caused by different methods of calculation of the atomic data and the ionization balance. OP calculated the atomic data by

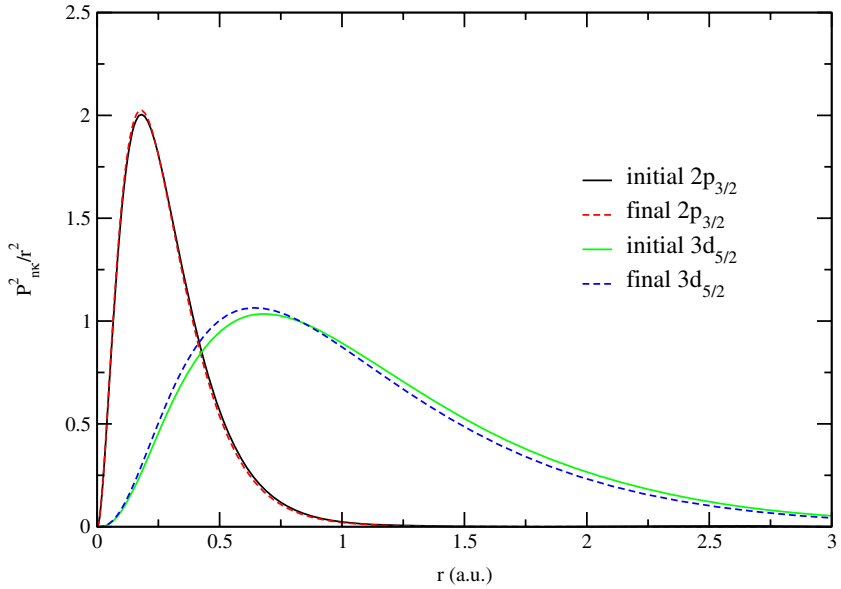

Figure 7. Radial wave functions of the initial and final $2p$ and $3d$ orbitals of the Fe VIII $2p \rightarrow 3d$ transition from the ground state.
(A color version of this figure is available in the online journal.)

using the R-matrix method in LS coupling. Unlike the present DLA, multi-CI effects are included in OP. However, CI effects could not lead to such large discrepancies between the two models. The differences of the population distributions calculated by the two methods should be the main reason for the discrepancies. Table 4 shows that the N_e of the DLA become smaller than those of OP. At densities of 0.18 and 0.63 g cm^{-3} Fe III–VIII are the main ions contributing to the opacity, and all of them have partially occupied $3d$ orbitals. The number of levels and lines of one charge state very different from those of the neighboring charge state. At $\rho = 0.18$ g cm^{-3} Fe IV, Fe V, Fe VI, and Fe VII are the main species in the plasma. The smaller N_e in the DLA indicates that it has more electrons in the M shell and therefore has more lines than OP. Thus the opacities in the DLA would be larger than those in OP. The IPD in Equation (17) is one important reason for such discrepancies in N_e. The IPD of one ion would cut the levels to a limited number. At high densities the IPD becomes large and can dramatically change the partition function of one ion and subsequently change its population in the plasma. If the IPD in the DLA is smaller than that in OP, the plasma in the DLA would be less ionized and more ions would populate the more highly excited states. That is to say, smaller IPDs would lead to more lines in opacity calculations. Since the package OPCD.3.3 does not provide charge state distributions in calculation, we cannot give more details for comparison between OP and our work. It is also worth noting that similar differences were also found in the comparison between OP and OPAL (Seaton &Badnell 2004).

We also calculated the Rosseland and Planck mean opacities with temperature ranging from 10 eV to 1000 eV and density ranging from 10^{-5} g cm^{-3} to 10^{-1} g cm^{-3}. The atomic data of each charge state were calculated. The principal quantum number n in the configurations was limited to $n \leqslant 9$. All lines including inner-shell excitations were calculated. In Equations (18) and (19) the upper bound of integration is limited to $u \leqslant 30$, i.e., 30 times the temperature in question. Since the weighting functions Equations (20) and (21) decrease exponentially at larger u, $u \leqslant 30$ is sufficient for Equations (18) and (19).

Table 3
Energies and Shifts of Some Fe VIII $2p \rightarrow 3d$ Transitions

Transition	ΔE_1	ΔE_2	Shift
$3d_{3/2}$-$\left[(2p_{3/2}^{-1}3d_{3/2})_3 3d_{5/2}\right]_{3/2}$	731.9	737.9	6.0
$3d_{3/2}$-$\left[(2p_{3/2}^{-1}3d_{3/2})_1 3d_{5/2}\right]_{5/2}$	733.9	739.8	5.9
$3d_{3/2}$-$\left[(2p_{1/2}^{-1}3d_{3/2})_2 3d_{5/2}\right]_{5/2}$	739.3	745.5	6.2
$3d_{3/2}$-$\left[2p_{1/2}^{-1}3d_{3/2}^2\right]_{3/2}$	745.6	751.3	5.7
$\left[3p_{3/2}^3(3d_{3/2}^2)_2\right]_{1/2}$-$\{\left[(2p_{3/2}^{-1}3p_{3/2}^3)_1 3d_{3/2}^2\right]_3 3d_{5/2}\}_{1/2}$	731.5	738.0	6.5
$\left[3p_{3/2}^3(3d_{3/2}^2)_2\right]_{1/2}$-$\{\left[(2p_{3/2}^{-1}3p_{3/2}^3)_1 3d_{3/2}\right]_3 3d_{5/2}^2\}_{1/2}$	741.6	747.4	5.8
$\left[3p_{3/2}^3(3d_{3/2}^2)_2\right]_{1/2}$-$\{\left[(2p_{1/2}^{-1}3p_{1/2}3p_{3/2}^4)_1 3d_{3/2}\right]_{5/2} 3d_{5/2}^2\}_{1/2}$	745.3	751.7	6.4
$\left[3p_{3/2}^3(3d_{3/2}^2)_2\right]_{1/2}$-$\{\left[(2p_{3/2}^{-1}3p_{3/2}^3)_1 3d_{3/2}^2\right]_2 3d_{5/2}\}_{1/2}$	749.1	755.3	6.2
$\left[3p_{3/2}^3(3d_{3/2})_1 3d_{5/2}\right]_{3/2}$-$\left[(2p_{3/2}^{-1}3p_{1/2})_1 3p_{3/2}^4 3d_{5/2}^3\right]_{3/2}$	731.9	738.5	6.6
$\left[3p_{3/2}^3(3d_{3/2})_1 3d_{5/2}\right]_{3/2}$-$\{\left[(2p_{3/2}^{-1}3p_{3/2}^3)_3 3d_{3/2}\right]_{9/2} 3d_{5/2}^2\}_{5/2}$	733.5	740.1	6.6
$\left[3p_{3/2}^3(3d_{3/2})_1 3d_{5/2}\right]_{3/2}$-$\{\left[(2p_{3/2}^{-1}3p_{3/2}^3)_2 3d_{3/2}^2\right]_0 3d_{5/2}\}_{5/2}$	735.3	741.8	6.5
$\left[3p_{3/2}^3(3d_{3/2})_1 3d_{5/2}\right]_{3/2}$-$\{\left[(2p_{3/2}^{-1}3p_{3/2}^3)_2 3d_{3/2}\right]_{1/2} 3d_{5/2}^2\}_{3/2}$	741.1	747.5	6.4

Note. The energies were calculated by considering (ΔE_1) and not considering (ΔE_2) orbital relaxation, respectively. All energies are in units of eV.

Figure 10 shows the mean charge states versus temperature at different densities. One can easily see that there are three steps, which correspond to the ionization thresholds of the M, L, and K shells, respectively. Taking the case of $\rho = 10^{-5}$ g cm^{-3} as an example, since the M-shell electrons have the smallest ionization energies, they are ionized rapidly with increasing temperature. When the temperature reaches 50 eV the M-shell electrons are almost fully ionized. However, ionization of the L-shell electrons needs more energy and stays frozen up to 70 eV. In the first step between 50 and 70 eV, Fe VII is the dominating ion with few neighboring charge states. When temperature increases above 70 eV, the L-shell electrons are quickly ionized until they reach the K-shell threshold. Because of the large ionization energies of the K-shell electrons the mean charge state has

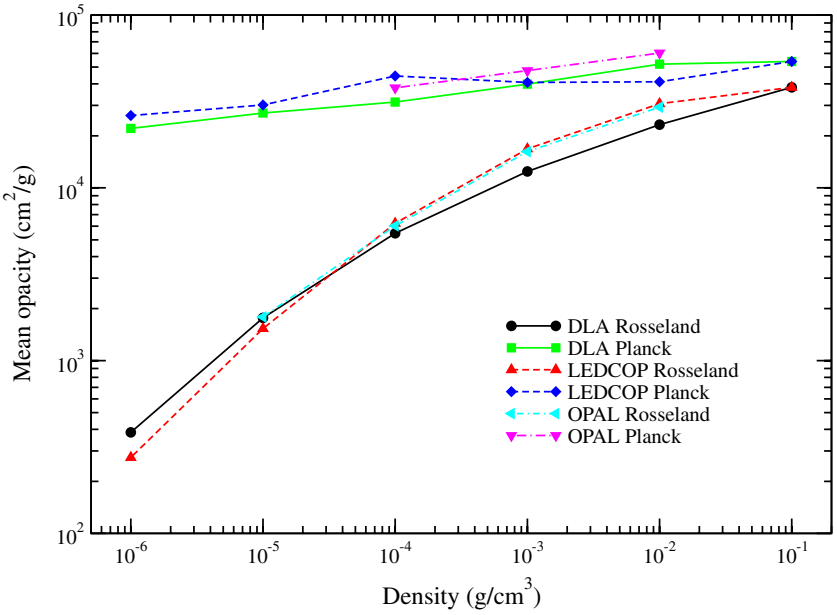

Figure 8. Rosseland and Planck mean opacities of isothermal series at 20 eV. The OPAL (Serduke et al. 2000; Richert 1995) and LEDCOP (Magee & Clark 1999) results are also plotted for comparison.

(A color version of this figure is available in the online journal.)

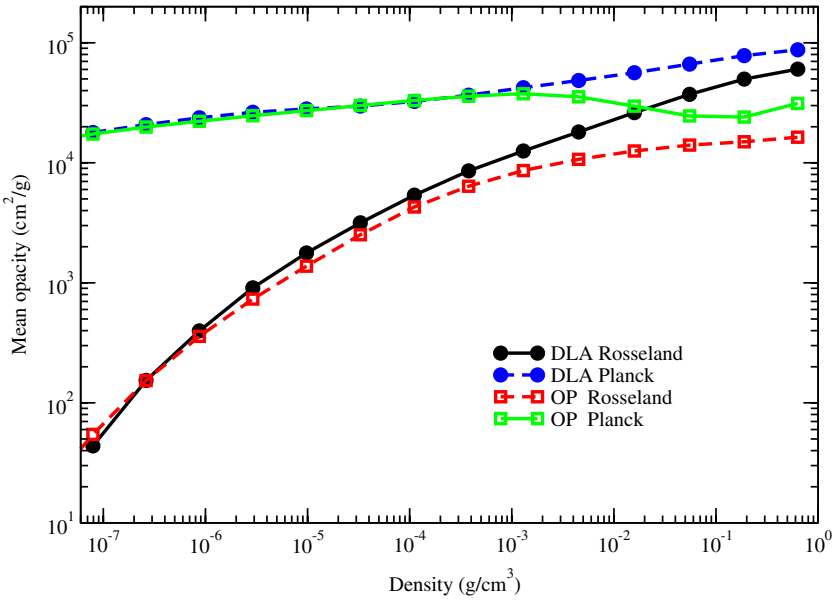

Figure 9. Comparison of the Rosseland and Planck mean opacities between OP and the present DLA for the isothermal series of $T = 19.3$ eV.

(A color version of this figure is available in the online journal.)

almost no change in the range 190–445 eV. After this step the *K*-shell electrons begin to be ionized. When the temperature reaches 650 eV the iron atoms are almost fully ionized. Only a few hydrogen-like ions remain.

In a hot plasma of a certain temperature an increase in density will make the ionization more difficult, and the distributions of the charge states will be broadened. In Figure 10, one can see that the growth of the mean charge state slows with increasing density. The steps are shortened and shifted toward higher temperatures. The slopes are also extended to broader ranges. The *M*- and *L*-shell steps at 10^{-1} g cm^{-3} are rather smoother than at 10^{-5} g cm^{-3}. Because of the large ionization energies of the *K*-shell electrons, the mean charge state is rather insensitive to density at temperatures around 400 eV.

Figure 11 shows the Rosseland and Planck mean opacities across a wide temperature and density range. In the figure, one can find valleys which correspond to the steps in Figure 10. We take the Planck mean opacity in the case $\rho = 10^{-5}$ g cm^{-3} as an example to show the behavior of the opacities with the temperature. The Planck mean opacity decreases rapidly with increasing temperature and reaches the minimum of the valley around 60 eV. In this stage the *M*-shell absorptions are the main contributions to the Planck opacities. At a temperature of 60 eV Fe XVII occupies 97.6% of the total populations

Table 4
The Electron Densities of an Isothermal Series at $T = 19.3$ eV Calculated by OP and DLA, Respectively

ρ	N_e (OP)	N_e (DLA)
7.90×10^{-8}	1.000×10^{16}	9.999×10^{15}
2.62×10^{-7}	3.162×10^{16}	3.165×10^{16}
8.72×10^{-7}	1.000×10^{17}	1.001×10^{17}
2.91×10^{-6}	3.162×10^{17}	3.167×10^{17}
9.76×10^{-6}	1.000×10^{18}	1.002×10^{18}
3.29×10^{-5}	3.162×10^{18}	3.171×10^{18}
1.11×10^{-4}	1.000×10^{19}	1.004×10^{19}
3.78×10^{-4}	3.162×10^{19}	3.175×10^{19}
1.30×10^{-3}	1.000×10^{20}	1.004×10^{20}
4.52×10^{-3}	3.162×10^{20}	3.186×10^{20}
1.59×10^{-2}	1.000×10^{21}	1.012×10^{21}
5.51×10^{-2}	3.162×10^{21}	3.170×10^{21}
1.89×10^{-1}	1.000×10^{22}	9.865×10^{21}
6.32×10^{-1}	3.162×10^{22}	3.033×10^{22}

Note. ρ is in g cm^{-3} and N_e in cm^{-3}.

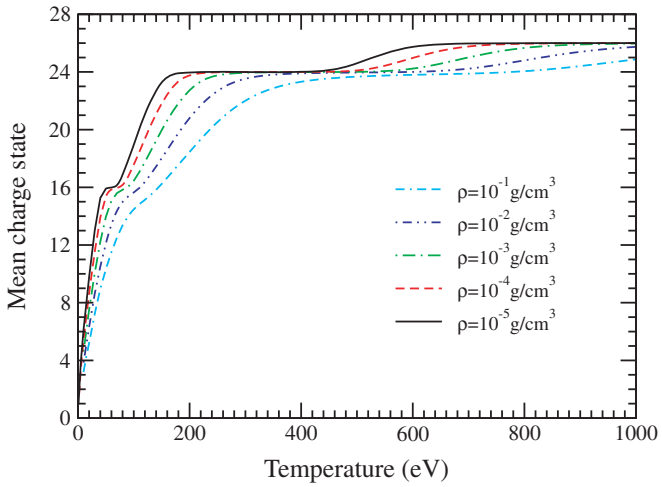

Figure 10. Mean charge state vs. temperature of iron plasma in the density range 10^{-5}–10^{-1} g cm^{-3}.
(A color version of this figure is available in the online journal.)

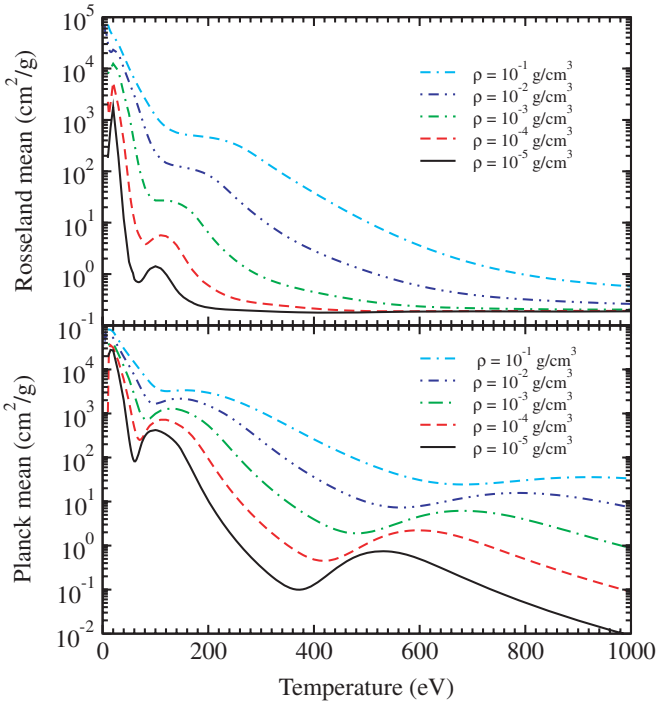

Figure 11. The Rosseland and Planck mean opacities of iron in the temperature range 10–1000 eV and the density range 10^{-5}–10^{-1} g cm^{-3}.
(A color version of this figure is available in the online journal.)

so there are almost no M-shell absorptions. Therefore, the Planck opacity reaches a minimum. With a continuous increase of temperature the contributions from the L-shell absorptions increase rapidly and reach a maximum at 100 eV. At this temperature the fractions of Fe XIX, Fe XX, and Fe XXI are 25.2%, 48.2%, and 21.5%, respectively. Thus the L-shell absorptions reach a maximum. When the temperature increases to 370 eV the Fe XXV fraction reaches 99.8% and the Planck opacity reaches a minimum. The last peak appears at 530 eV, where the Fe XXVI fraction reaches its maximum 60.4%. As the density increases the Planck opacities increase, and the sharp valleys are stretched at high densities. The Rosseland opacity behavior is similar to the Planck opacity except that the peak around 530 eV is very small and not obvious. The reason is that photon scattering by free electrons become comparable with the K-shell absorptions when the L-shell electrons are fully ionized. With the continuous ionization of the K-shell electrons the photon scattering dominates the opacities and the Rosseland opacity tend to be a constant.

Figure 12 shows the comparison between the DLA and LEDCOP for the mean opacities at 10^{-4} g cm^{-3} and in the temperature range 10–1000 eV. The Rosseland opacities of the two models agree well below 50 eV and above 300 eV. The disagreements in the range 50–300 eV may be due to the UTA treatments to the L-shell lines in the LEDCOP code. Large disagreement is also found in the Planck opacities above 250 eV. One reason is that although the two codes are detailed line models, they are different in the calculation of the atomic levels, transition arrays, partition functions, populations, and so on. Such differences are critical at high temperatures, where the absorptions of neighboring charge states are quite different. Another possible reason is that we obtained the LEDCOP opacities via the online opacity server of LANL through the internet. The logarithmic energy grid of the download opacities would be sparse at high photon energies. Inadequate energy grids could cause errors at high temperatures, where the L- and K-shell lines dominate the opacities.

In many applications, statistical models such as AA, UTA, and STA are usually used to generate large number of opacities rapidly. This is especially important in studies of high-Z materials. However, the accuracy of statistical models should be validated. In general, DLA calculations have higher accuracy due to the detailed treatment of the transition lines, and they could be taken as a benchmark for statistical models. Figure 13 shows the comparison between the DLA and an AA model (Yuan 2002a, 2002b). One can see that the Planck opacities calculated by the two models agree quite well at the higher density of 10^{-2} g cm^{-3} and at the lower density of 10^{-4} g cm^{-3}. This insures that the total transition probabilities calculated by the two models at a certain temperature are the same. However, the Rosseland opacities calculated by the AA model are systematically larger than those of the DLA model particularly around 80 eV. In the AA model, all the ions of different charge states and configurations are averaged into a fictitious atom with shell structures, and the electrons are distributed

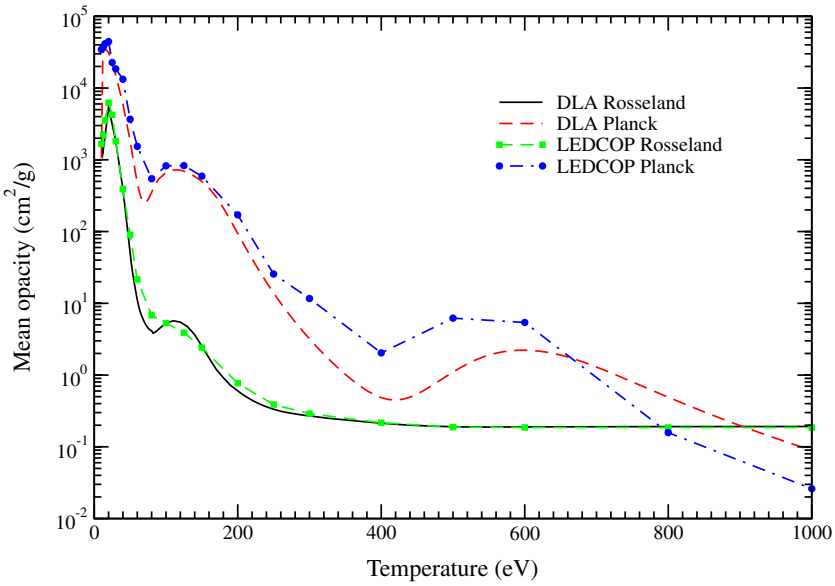

Figure 12. Comparisons between our DLA and the LEDCOP (Magee & Clark 1999) for the Rosseland and Planck mean opacities of iron at 10^{-4} g cm^{-3} and in the range 10–1000 eV.

(A color version of this figure is available in the online journal.)

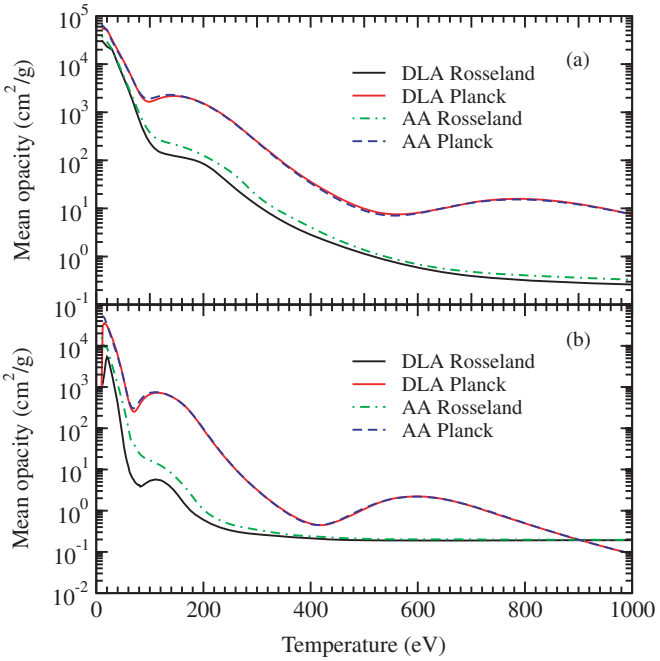

Figure 13. Comparisons between the present DLA and an AA model (Yuan 2002a) for the Rosseland and Planck mean opacities of iron. The plasma density in (*a*) is 10^{-2} g cm^{-3} and in (*b*) is 10^{-4} g cm^{-3}.

(A color version of this figure is available in the online journal.)

to the shells according to the Fermi–Dirac distribution rule. The AA model replaces the actual transition arrays of different ions by transitions between the shells of the average atom. Figure 14 shows the comparison of the spectrally resolved opacities between the DLA and the AA models. The AA model grouped and smoothed the DLA transition arrays and therefore overestimated the Rosseland opacities. With increasing density, the Stark broadening would increase rapidly and lead to overlaps between the neighboring lines in the DLA spectrum. In Figure 14(a), the DLA spectrum has a less detailed structure and is closer to the AA spectrum. At 10^{-4} g cm^{-3} the AA Rosseland opacity is 24.9 cm^2 g^{-1}, which is much larger than the 4.1 cm^2 g^{-1} of the DLA model. When the density increases to 10^{-2} g cm^{-3} the AA Rosseland opacities is 966.9 cm^2 g^{-1} which is close to the 702.2 cm^2 g^{-1} of the DLA model. In Figure 13, one can see that the two models agree better at higher density, especially below 80 eV.

In summary, we have developed a DLA model to study the opacities of LTE iron plasmas. The atomic data were generated by solving the full relativistic Dirac–Fock equations. Only state mixing within one configuration is considered to avoid over-large CI matrices. Several recent experimental transmission spectra in the *M*- and *L*-shell absorption regions are simulated to validate our model. Quite good agreement was found between our calculations and the experiments, although some discrepancies still exist. At low temperatures of about 20 eV, the calculated absorptions of some $3p \rightarrow 3d$ transitions without enough correlation effects are larger than shown by experiment. The calculated $2p \rightarrow 3d$ line energies are systematically 6.5 eV larger than in experiment since the orbital relaxations of inner-shell electrons have not been considered in the present model. The present model is also compared with the OPAL, LEDCOP, and OP models for two isothermal series at $T = 20$ eV and $T = 19.3$ eV. It is found that the present model in good agreement with OPAL and LEDCOP while it has discrepancies with OP at high densities. Rosseland and Planck mean opacities in the temperature range 10–1000 eV and density range 10^{-5}–10^{-1} g cm^{-3} are calculated and compared with the LEDCOP results. Good agreement is found at lower temperatures but differences appear at high temperatures where the *L*- and *K*-shell absorptions are dominant. Comparison between the DLA and AA models is also made to show that the Rosseland mean opacities calculated by the AA model at higher density are in good agreement with the DLA model. From the discussions we conclude that for iron plasma, which is a typical medium-*Z* material and requires complicated calculation of the huge number of atomic data, the present DLA model obtained good agreement with experimental data and some other theoretical models; however, further studies, such as on CI effects, orbital relaxation effects, and population distributions, should be performed in future works.

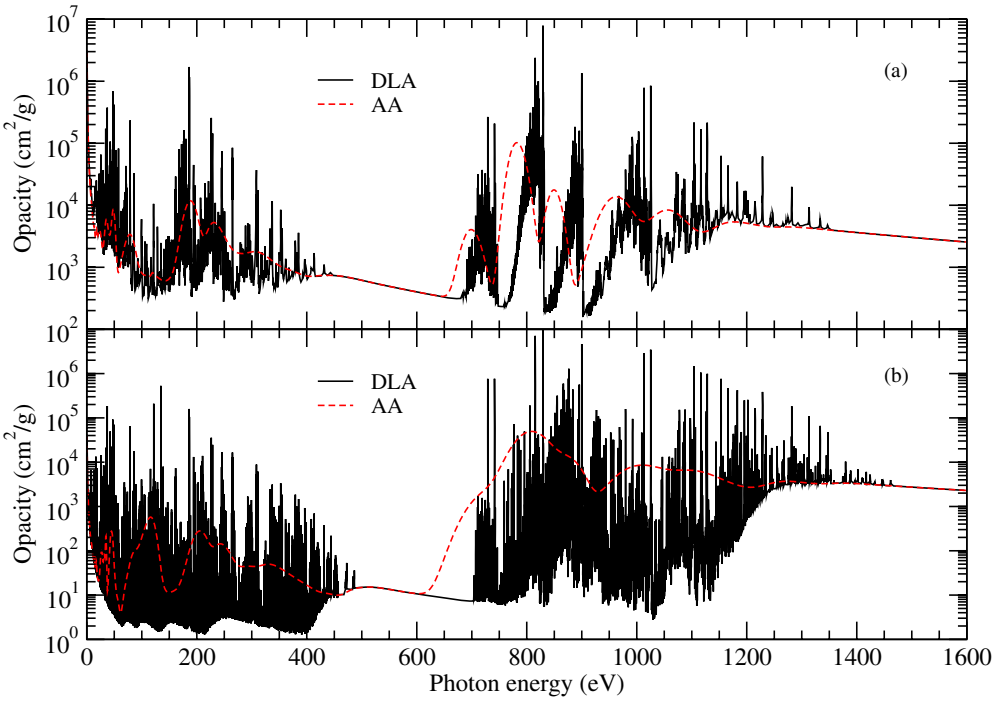

Figure 14. Spectrally resolved iron opacities calculated by DLA and AA models (Yuan 2002a) at the same temperature, 80 eV. The densities in (*a*) and (*b*) are 10^{-2} g cm^{-3} and 10^{-4} g cm^{-3}, respectively.

(A color version of this figure is available in the online journal.)

This work was supported by the National Natural Science Foundation of China under grant Nos. 10604067 and 10734140, the National Basic Research Program of China (973 Program) under grant No. 2007CB815105, and the National Key Laboratory Foundation under contract No. 9140C6804010805.

REFERENCES

Badnell, N. R., Bautista, M. A., Butler, K., Delahaye, F., Mendoza, C., Palmeri, P., Zeippen, C. J., & Seaton, M. J. 2005, MNRAS, 360, 458
Bailey, J. E., et al. 2007, Phys. Rev. Lett., 99, 265002
Bauche, J., Bauche-Arnoult, C., & Perusse, O. 2006, J. Quant. Spectrosc. Radiat. Transfer, 99, 55
Bell, R. A., Balachandran, S. C., & Bautista, M. 2001, ApJ, 546, L65
Busquet, M. 1993, Phys. Fluids B, 5, 4191
Castelli, F., & Kurucz, R. L. 2004, A&A, 419, 725
Chenais-Popovics, C., et al. 2000, ApJS, 127, 275
Corliss, C., & Suger, J. 1985, J. Phys. Chem. Ref. Data, 11, 135
Cowan, R. D. 1981, The Theory of Atomic Structure and Spectra (Berkeley, CA: Univ. California Press)
Cox, A. N., & Tabor, J. E. 1976, ApJS, 31, 271
Dimitrijevic, M. S., & Konjevic, N. 1987, A&A, 172, 345
Fontes, C. J., Colgan, J., Zhang, H. L., & Abdallah, J., Jr. 2006, J. Quant. Spectrosc. Radiat. Transfer, 99, 175
Foord, M. E., et al. 2004, Phys. Rev. Lett., 93, 055002
Hummer, D. G., Berrington, K. A., Eissner, A. K. P., Saraph, H. E., & Tully, J. A. 1993, A&A, 279, 298
Iglesias, C. A., & Rogers, F. J. 1996, ApJ, 464, 943
Jin, F., Zeng, J., & Yuan, J. 2003, Phys. Rev. E, 68, 066401
Klapisch, M., & Bar-Shalom, A. 1997, J. Quant. Spectrosc. Radiat. Transfer, 58, 687
Magee, N. H., & Clark, R. E. H. 1999, http://www.t4.lanl.gov
Parpia, F. A., Fischer, C. F., & Grant, I. P. 1996, Comput. Phys. Commun., 94, 249
Richert, A. 1995, J. Quant. Spectrosc. Transfer, 54, 325
Rogers, F. J., & Iglesias, C. A. 1992, ApJS, 79, 507
Rogers, F. J., & Iglesias, C. A. 1994, Science, 263, 50
Rose, S. J. 1992, J. Phys. B, 25, 1667
Rose, S. J., et al. 2004, J. Phys. B, 37, L337
Seaton, M. J. 1987, J. Phys. B At. Mol. Phys., 20, 6363
Seaton, M. J., & Badnell, N. R. 2004, MNRAS, 354, 457
Seaton, M. J., Yan, Y., Mihalas, D., & Pradhan, A. K. 1994, MNRAS, 266, 805
Serduke, F. J. D., Minguez, E., Davidson, S., & Iglesias, C. A. 2000, J. Quant. Spectrosc. Radiat. Transfer, 65, 527
Simon, N. R. 1982, ApJ, 260, L87
Springer, P. T., et al. 1997, J. Quant. Spectrosc. Radiat. Transfer, 58, 927
Stewart, J. C., & Pyatt, K. D. 1966, ApJ, 144, 1203
Winhart, G., Eidmann, K., Iglesias, C. A., & Bar-Shalom, A. 1996, Phys. Rev. E, 53, R1332
Winhart, G., Eidmann, K., Iglesias, C. A., Bar-Shalom, A., Minguez, E., Rickert, A., & Rose, S. J. 1995, J. Quant. Spectrosc. Radiat. Transfer., 54, 437
Xu, X. 1986, Introduction to Practical Theory of EOS (Beijing, China: Science Press) (in Chinese)
Yuan, J. 2002a, Chin. Phys. Lett., 19, 1459
Yuan, J. 2002b, Phys. Rev. E, 66, 047401
Zeng, J., Jin, F., Zhao, G., & Yuan, J. 2003, J. Phys. B, 36, 3457
Zeng, J., & Yuan, J. 2004, Phys. Rev. E, 70, 027401